Elastic properties and heterogeneous stiffness of the Phi29 motor connector channel

Rajendra Kumar and Helmut Grubmüller
Max Planck Institute for Biophysical Chemistry,
Department of Theoretical and Computational Biophysics,
Göttingen, 37077, Germany

Supporting Material

Contents

Sections

Tables

Figures

References

1. Description of connector loops modeling and refinement

The connector loops A230-S244 were unresolved in the X-ray crystal structure (Fig. S1A) and therefore modeled as follows. First, an initial structure model was obtained for one of the twelve symmetry-related missing loops using the ArchPred server (1). This seed structure was then replicated (according to the 12-fold symmetry of the connector) and manually integrated within all other remaining sub-units after aligning the seed structure (see Fig. S1B). In addition, four of the twelve subunits of the connector lacked residues (Q166-L169) in the bottom region. These residues were modeled using Modeller program (2) by taking a template subunit in which these residues are present.

Also, in a structure of the connector in complex with DNA, the diversity in DNA-loop interactions will cause the 12 connector loop structures to slightly differ from each other because of the lack of 12-fold symmetry in the DNA helical grooves. To model this structural heterogeneity, all 12 connector loops were refined by a combined simulated annealing and molecular dynamics (SA/MD) protocol as described in following.

First, the viral DNA of the Phi29 bacteriophage gp10 gene (NCBI Reference Sequence: NC_011048.1) was modeled into the connector channel center. The first 60 nucleotides (ATG GCA CGT AAA CGC AGT AAC ACA TAC CGA TCT ATC AAT GAG ATA CAG CGT CAA AAA CGG) were modeled as B-DNA strand using the Nucleic Acids Builder NAB (3) and is depicted as *yellow* and *blue* ring (top view) in Fig. S1B.

Next, the initial molecular system was prepared for the Simulated Annealing Molecular Dynamics (SA MD) simulations: The connector-DNA complex was set in the center of a dodecahedron periodic box, solvated with 241,067 water molecules, and neutralized by addition of a sufficient number of Sodium ions (in total 202). The system was energy-minimized and subsequently heated during a NVT simulation of 500 ps with a 1 fs time step. Pressure was equilibrated during a subsequent NPT simulation of 1 ns with a 2 fs time step. In both simulations, the positions of all heavy atoms were restrained by an harmonic force constant of 1000 kJ/(mol nm^2). 40 SA cycles of 252 ps length were performed for 10 ns during the SA MD simulations. In each SA cycle, the loops were heated up in two steps to a temperature of 1000 K and subsequently cooled down in seven steps to 300 K (Table S1). Only the loops were free to

move during the SA MD simulations, whereas other heavy atoms of the connector-DNA complex were restrained at the starting position by a force constant of 1000 kJ/(mol nm^2) to preserve the structure of the complex at high temperatures.

The SA MD and below described cooling simulations were performed using the GROMACS 4.0.7 package (4), in which AMBER ff99SB (5) and parmbsc0 (6) force fields were used for connector and DNA, respectively. The temperature was regulated during heating and cooling by Berendsen temperature coupling, whereas the pressure was maintained at 1 atm by the Berendsen pressure coupling (7). Long range electrostatic interactions were computed by applying the PME method with a grid spacing of 1.2 Å and a 4th order of cubic interpolation (8). Short range non-bonded interactions were computed for the atom pairs within a distance of 10 Å. The temperature used in SA MD simulations flattened the energy landscape and facilitated random changes in loop conformations that were collected during 10 ns. To assess the convergence of loop conformations during MD simulations, principal component analyses (PCA) were performed (9-13) on the last 6 ns of each SA MD trajectory. The first two principal components (PC) were used because these have the largest variance and hence show the largest conformation changes.

Figure S2A shows the two-dimensional plane of the first PC with respect to the second PC. The semi-circle shape of the plane reveals randomness in conformations along the first two PCs (14). The obtained high temperature conformations (red dots in Fig. S2A) are most likely located at a high energy region on the free energy landscape and were not used for MD simulations. However, cooling of these conformations is expected to allow achieving nearest free energy minimum loop conformations. To this aim, five different high temperature conformations were chosen from the projection planes of PC1 and PC2 (A, B, C, D and E in Fig. S2A). These conformations were cooled from 1000 K down to 300 K in 6 ns and subsequently equilibrated for 1 ns at 300 K in a NPT simulation (cooling simulations). Finally, five clusters of structures were obtained (A′, B′, C′, D′ and E′ in Fig. S2A) at 300 K. These were compared by computing root mean square deviations (RMSD) of C-alpha atoms of the loops with respect to the initial structure model (five different blue symbols in Fig. S2B) and found to be within 0.2 nm difference. The deviation is not significant for these highly flexible loops. Consequently, the central structure from this cluster was used for further studies. The final loop conformations and DNA-loop interactions are illustrated in Fig. S2C.

2. Structural and conformational equilibration of the connector

We monitored the structural stability of the connector during equilibrium MD simulations via root mean square deviation (RMSD) calculated for C-alpha atoms with respect to the crystal structure (Fig. S7). After an initial sharp rise during the first 10 ns, the RMSD-values stabilize at about 0.25 nm during the subsequent 190 ns. Averaged over the last 190 ns of the equilibration phase, a twist angle of $\theta = 77.7°$ and a length of L = 4.89 nm was obtained, with a standard deviation of 0.4° and 0.04 nm, respectively (Fig. 2A). Because of the RMSD drift observed during the first 100 ns, average values were also computed for the last 100 ns, and a similar twist angle ($\theta = 77.6°$) and length ($L = 4.91$ nm) were obtained. Whereas the connector length remained at that of the crystal structure ($L = 4.91$ nm), the twist angle increased by ca. 3.5^o with respect to the crystal structure ($\theta = 74.2^o$) during the first 10 ns. Closer inspection showed that the deviation was actually due to an increased tilt of the helices as depicted in Fig. S8, and in particular those helices which are in contact with symmetry mates in the crystal structure. This increased tilt of those helices slightly shifted the center of mass of the bottom region of each subunit that was used to calculate the twist angle (see Figs. 1C and D). We therefore assume that this tilt in the crystal structure is due to crystal contacts between these alpha helices and the upper region. The structures of the middle and upper regions are largely unaffected. Given the size of the connector, we consider the observed RMSD of ca. 0.25 nm and the underlying structural changes during equilibration rather small. Because the overall structure and the RMSD remained unchanged during the last 100 ns, this part of the trajectory was used for further analysis.

5

3. Elastic properties determined from force-probe simulations

3.1. Methods

3.1.1. Force probe MD simulations

To study the mechanical properties of the connector by force probe simulations, the structure was subjected to external forces via two structural descriptors (see Fig. 1D), the twist angle θ_m which describes the twisting-untwisting motion of the middle region of the connector, and its length L_m, which quantifies the compression-stretching motion of the middle region. The upper and lower disk in Fig. 1E represents Cα atom from the upper- and lower-terminus of MH1 and MH2 helices of each subunit, respectively. We will refer to the atoms of the lower and upper disk as pull or rotational group and reference group in the subsequent sections, respectively. Rotation between two disks defines the twisting-untwisting motion while motion of disks along channel axis shows the compression-stretching motion.

Six force-probe MD simulations (FP-1, FP-2, FP-3, FP-4, FP-5 and FP-6) were performed to investigate the twisting-untwisting and compression-stretching motions of the connector beyond the equilibrium fluctuations (see details in Table. S2). All force probe simulations started from the equilibration trajectory after 25 ns. To drive the compression and stretching motion, the center of mass of the pull group (lower disk in Fig. 1D) was moved away (stretching) and towards (compression) the center of mass of the reference group (upper disk in Fig. 1D). To drive the untwisting and twisting motions, the atoms of the rotational group (lower disk in Fig. 1D) were forced to move along circles centered at the z-axis by applying a torque potential in both anti-clock wise (untwist) and clock wise (twist) direction, respectively (grey arrow in Fig. 1D). At the same time, the center of mass of the reference group was kept fixed by a harmonic restraint of 1000 kJ/(mol nm^2). As defined in Ref. (15) the variant *rm2-pf* was chosen as rotational potential, which allowed the radial motion of the rotational group atoms (15). All simulations were carried out using a modified version of GROMACS in which rotational pulling was implemented (15). The total simulation time was ~160 ns.

3.1.2. Relaxation simulations

To study within which regime the observed deformation is reversible and hence elastic, two intermediate structures of 5.1 and 5.3 nm length, were chosen from the FP-6 simulation (see

Figs. S3B and C) for subsequent relaxation simulations (Relax-1 and Relax-2, respectively). To equilibrate the structure at the starting twist angle and length, all atoms of pull and reference group were restrained by force constant of 1000 kJ/(mol nm^2) for the first 4.4 ns. The force was then removed, and the connector was allowed to relax freely, during which period the approach to its equilibrium length and twist angle was monitored. Furthermore, to check the structural reversibility of the compressed connector, an intermediate representative structure of the connector with a middle region's length L_m=2.7 nm was taken from the 7.52 ns of the FP-5 simulation (see Fig. S3A) for a subsequent relaxation simulation (Relax-3). At this specific snapshot of the FP-5 trajectory, the length L_m=2.699 nm was nearest to the required value of L_m=2.7 nm. In this relaxation simulation, the connector was kept at its enforced twist angle and length for 3.3 ns before the pulling and restraint potentials were removed in order to allow relaxation towards its equilibrium length. An additional relaxation simulation (Relax-4) was performed from FP-6 simulation to obtain relaxed structures of the connector which was later used for the umbrella sampling simulations.

3.2. Results and discussion

In the first set of simulations (FP-1 and FP-2), the connector was compressed and stretched by applying linear pulling forces as described in the methods section (Fig. 1D and Table S2). The required forces as well as the resulting connector twist angle θ as a function of connector length L was observed (Fig. S10A, red symbols). Indeed, for the range accessible to equilibrium fluctuations (black ellipse) as well as for larger compressions beyond the equilibrium fluctuations (left branch of the curve), the connector's twist angle changes by 2°/nm (Table S6), and is herewith similar to the one determined above (dashed line in Fig. S10A). Up to the maximum exerted force of 5000 pN, and at a compression by ca. 4%, the force extension curve (Fig. S10B, red line) is linear, indicating Hookean behavior within this range.

For stretching beyond the equilibrium range (outside of ellipse in Fig. S10A), an unexpectedly large untwisting is observed, by 13.5°/nm up to 5.1 nm length, with a continued linear (Hookean) force. Beyond that critical force, the structure started to break down, which is also reflected in the decreased slope of the force extension curve and may indicate non-elastic behavior. Interestingly, the coupling between extension and untwisting remains linear also beyond the

critical force. Within the Hookean regime, a spring constant of ~27200 pN/nm (red line in Fig. S10B) is observed.

The large untwisting motion beyond $L=5.05$ nm is unexpected because non-equilibrium relaxation would likely make the untwisting lag behind its equilibrium pathway (dashed curve in Fig. S10A), in contrast to the observed increased slope. Note, however, that this additional untwisting is solely due to structural re-arrangements of the bottom region of the connector, which is not subjected to the pulling force (cf. inset in Fig. S10A). Indeed, the untwisting motion of the middle region alone displays linear coupling up to full extension (see red line Fig. S11A). It remains to be tested whether or not this linear pathway resembles the equilibrium path.

In a second set of FP simulations (FP-3 and FP-4), the connector was twisted and untwisted by applying a torque (see Methods Section), and the required torque as well as the length change as a function of twist angle was monitored (blue symbols, Figs. S10A and C). Beyond the equilibrium fluctuations, the connector twist angle θ changed linearly with length L by 27.9°/nm, markedly larger than that calculated from equilibrium fluctuations (Table S6). By exceeding an untwisting of 70° the structure started to break down. The torque-angle curve (blue line, Fig. S10C) is Hookean between 75° and 78°, with a torsional spring constant of ~3500 pN nm/$^\text{o}$.

In all of the above simulations (FP-1 to FP-4), the obtained stretching and torsional spring constants were larger than those derived from equilibrium simulations. We assume this discrepancies to be caused by non-equilibrium effects in force probe simulations, which are absent in equilibrium simulations. Specifically, during the relatively short time of about ten nanoseconds for each simulation, relaxation is likely to be incomplete for several of the internal degrees of freedom of the connector, as previously described and quantified in terms of a two-dimensional time-dependent transition state theory also for the connector (16). In this scenario, as a result of this incomplete relaxation, the twist angle θ should 'lag behind' (i.e., larger θ values) a fully equilibrated pathway along the minimum ('valley') of the underlying untwisting-stretching free energy landscape. Vice versa, when untwisting the connector (blue symbols, Fig. S10A), the length expansion is expected to lag behind, which explains why this untwisting-stretching curve falls below that of the stretching simulations. Accordingly, the equilibrium pathway is expected in between these two extremes.

We tested this hypothesis by performing several relaxation simulations, starting from different points along the stretching and untwisting simulations, in which the pulling force or torque, respectively, was removed. If relaxation effects dominate the observed differences between stretching and untwisting, one would expect the relaxation trajectories to deviate from the force probe trajectories and to converge towards their common equilibrium pathway. Indeed, Fig. S12 clearly shows such convergence. Both twist angle and length changed rapidly towards an intermediate pathway, and almost reach an equilibrium region within ca. 10 to 20 ns. Notably, the slope of the converged line is larger than that of the equilibrium coupling, which suggests that the coupling mechanism between length change and untwisting outside the equilibrium region differs from that in thermal equilibrium.

To approximate this equilibrium path, which will also be used for subsequent deformation free energy calculations, two further force probe simulations (FP-5 and FP-6) were performed in which both stretching forces and torque were applied simultaneously. Because the above relaxation simulations suggest that the equilibrium path is located approximately right in between the paths probed by simulations FP 1-2 and 3-4, respectively, the same ratio between pulling and rotation speed was chosen here. To allow for more complete relaxation, a ten times reduced pulling force and torque rate (Table S2) was used.

The obtained length and twist angle changes are shown in Fig. S10A (green symbol). As expected, the resulting deformation pathway falls right in between the paths obtained in the stretching-only, untwisting-only and relaxation simulations. As an example, movie S1 shows an animation of trajectory FP-6. Linear coupling is observed, with a coupling coefficient of 18°/nm throughout the whole stretching/untwisting process (green line in Fig. S10A). Also in these simulations, structural break-down occurred at L = 5.15 nm (shown in movie S2). No linear coupling between compressions and twisting is observed; rather, the twist angle saturates at 79.5° during compression. Within the regime of equilibrium fluctuations, Hookean behavior of both the stretching and untwist is observed (Figs. S10B and C, green symbols), with stretching and torsional spring constants similar (Table S6) to those obtained from simulations FP-1/2 and FP-3/4, respectively. For extensions exceeding 5.0 nm length and twist angle below 76°, respectively, non-Hookean behavior sets in. Remarkably, the change of the connector's

mechanical properties is very abrupt at this critical deformation, with no additional torque being required for further large connector untwisting.

To test whether the observed non-Hookean behavior also implies non-elastic behavior for both the untwisting-stretching motion as well as the observed structural break-down, we have carried out further relaxation simulations (see methods section), starting from non-equilibrium conformations extracted from simulations FP-5 and FP-6 at lengths L of 4.75, 5.1, and 5.3 nm, respectively (the corresponding structures are shown in Fig. S3). Figure S13A shows the obtained relaxation motions in terms of both length L and twist angle θ during the final part of the restrained simulation (left of the dashed line) and after removal of the restraining potential (right of dashed line). The equilibrium values are regained in all three simulations. Even the extreme non-Hookean deformation of up to L = 5.3 nm length approaches the equilibrium value after 100 ns, despite the structural deformations shown in Fig. S3C (shaded box) and Movie S2, which demonstrates that the connector is able to recover its equilibrium structure even after structural break down. As can be seen in Figs. S13B and C, all three relaxation trajectories remain close to the untwisting/stretching paths of simulations FP-5 and FP-6, which underscores that these simulations remained close to the 'valley' of minimal perturbation.

Overall, deformations within the range of L = 4.70-5.3 nm and θ = 70°-79.5° seem to be fully elastic, and the twisting-untwisting motion is linearly coupled to the compression-stretching motion within this elastic range. The obtained coupling of 18°/nm is remarkably close to the coupling of 17.6°/nm required in the untwist-twist DNA packaging model proposed by Simpson et al. (17). We therefore asked next if also the other elastic and energetic properties of the connector are compatible with this model.

Tables

Table S1: Heating-cooling cycles performed in SA MD simulations. The connector loops were heated up and cooled down consecutively 40 times during 10 ns of MD simulations. Each cycle consisted of 252 ps with two and eight steps of heating and cooling, respectively.

Temperature (K)	Time period (ps)	Cumulative time (ps)
300	20	20
300-600	2	22
600	22	44
600-1000	2	46
1000	50	96
1000-800	2	98
800	20	118
800-700	2	120
700	20	140
700-600	2	142
600	20	162
600-500	2	164
500	20	184
500-450	2	186
450	20	206
450-400	2	208
400	20	228
400-350	2	230
350	20	250
350-300	2	252

Table S2: Force rates and torque/force constants applied in FP simulations. Corresponding simulation names are used throughout the main article and the supplementary text.

Name	Force probe simulations (along motion type)	Rate		Force constant [kJ/(mol nm^2)]	
		Rotational (°/ps)	Pulling (nm/ps)	Rotational	Pulling
FP-1	Compression*	—	0.010	—	100
FP-2	Stretching*	—	0.010	—	100
FP-3	Twisting*	0.0040	—	500	—
FP-4	Untwisting*	0.0040	—	500	—
FP-5	Twisting and compression	0.0004	0.001	500	100
FP-6	Untwisting and stretching	0.0004	0.001	500	100

*These simulations were performed three times in parallel.

Table S3: Details of compression-stretching umbrella sampling simulations. The simulation type from which the reference starting conformation for each sampling window was extracted is denoted accordingly. The frame time corresponds to the time of the reference simulation from which the reference structure was taken. The relaxation simulations Relax-1, Relax-2, Relax-3, and Relax-4 were performed using the non-equilibrium starting structures from simulations FP-5 and FP-6.

Sampling window	Reference simulation type	Frame time (ps)	Reference reaction coordinate, L_m (nm)	Force constant [kJ/(mol nm^2)]
1	Relax-3	3300	2.725	2500
2	Equilibrium	107000	2.750	500
3	Equilibrium	74200	2.800	500
4	Relax-1	16940	2.850	2500
5	Relax-1	4460	2.876	5000
6	Relax-2	16420	2.900	7500
7	Relax-2	8000	2.950	7500
8	Relax-2	5320	2.997	10000
9	Relax-2	4720	3.025	15000
10	Relax-2	4580	3.052	15000
11	Relax-4	5200	3.075	17500
12	Relax-4	5140	3.100	20000
13	Relax-4	5060	3.125	20000
14	Relax-4	5040	3.149	20000

Table S4: Details of twisting-untwisting umbrella sampling simulations. The simulation type from which the reference starting conformation for each sampling window was extracted is denoted accordingly. The frame time corresponds to the time of the reference simulation from which the reference structure was taken.

Sampling window	Reference simulation type	Frame time (ps)	Reference reaction coordinate, $\theta_m°$	Force constant [kJ/(mol.nm^2)]
1	FP-6	24700	29.55	10000
2	FP-6	24090	30.02	7500
3	FP-6	22880	30.50	6000
4	FP-6	21570	31.01	5000
5	FP-6	18520	31.57	5000
6	FP-6	18310	32.02	2500
7	FP-6	12522	32.44	2500
8	FP-6	11362	33.13	1000
9	FP-6	8772	33.45	500
10	FP-6	7042	33.90	500
11	FP-5	1576	34.50	1000
12	FP-5	5566	35.00	6500
13	FP-5	9748	35.50	6500
14	FP-5	11030	36.00	10000

Table S5: Dimensions of the connector and its middle region used to calculate the Young's modulus of elasticity. Values were obtained from equilibrium MD simulations using Eq. 4. Notations are in accordance with labels used in the truncated cone sketch shown in Fig. S6. Given error represents the SE obtained using the block-averaging method (18).

Connector region	D_a [nm]	D_b [nm]	d_a [nm]	d_b [nm]	L [nm]
Whole connector	6.259 ± 0.015	14.720 ± 0.012	4.229 ± 0.103	5.866 ± 0.011	6.578 ± 0.025
Middle region	5.194 ± 0.044	9.268 ± 0.012	3.668 ± 0.028	7.188 ± 0.005	2.861 ± 0.002

Table S6: Mechanical properties of the whole connector and its middle region. Equilibrium mechanical properties were obtained using Eq. 2. Best-fit lines within the linear regime are depicted in Figs. S10B, S10C, S11B and S11C. Couplings between untwisting-stretching motions were obtained in a similar manner and are shown in Figs. 2, S10A and S11A.

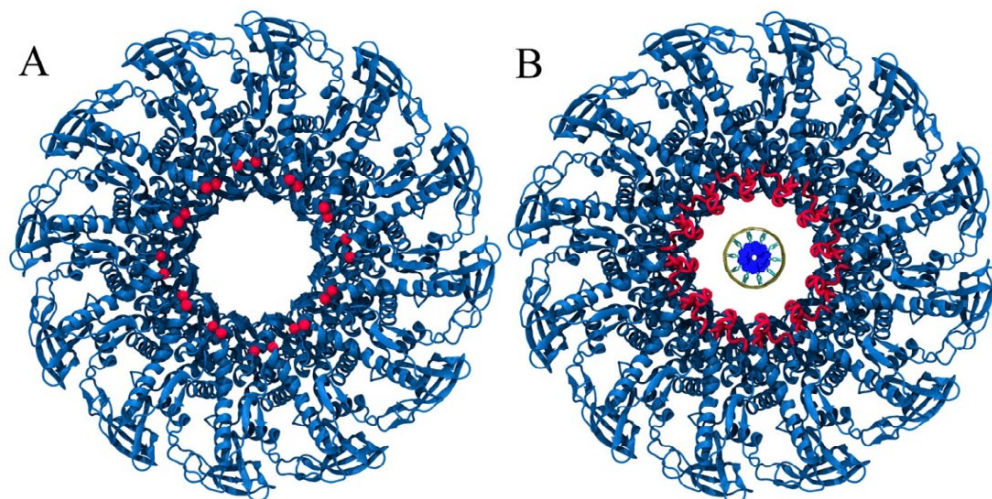| Simulation type	Connector region	K_θ [(pN nm)/Deg^2]	K_L [pN/nm]	K_c [pN/Deg]	Coupling (Deg/nm)
Equilibrium	Whole connector	1347	3073	2715	2.0
	Middle region	3374	24109	14848	4.4
FP 1 and 2	Whole connector	—	27204	—	2.0 and 13.5
	Middle region	—	33437	—	4.2
FP 3 and 4	Whole connector	3558	—	—	27.9
	Middle region	3404	—	—	51.3
FP 5 and 6	Whole connector	3033	27747	—	18.1
	Middle region	3428	28282	—	17.7

Figures

Figure S1: Crystal structure of the connector in top view. (A) Red spheres denote the location of the missing loops. (B) Modeled loops (*red*) are not in contact with the DNA (*yellow* and *blue* ring at the center of channel).
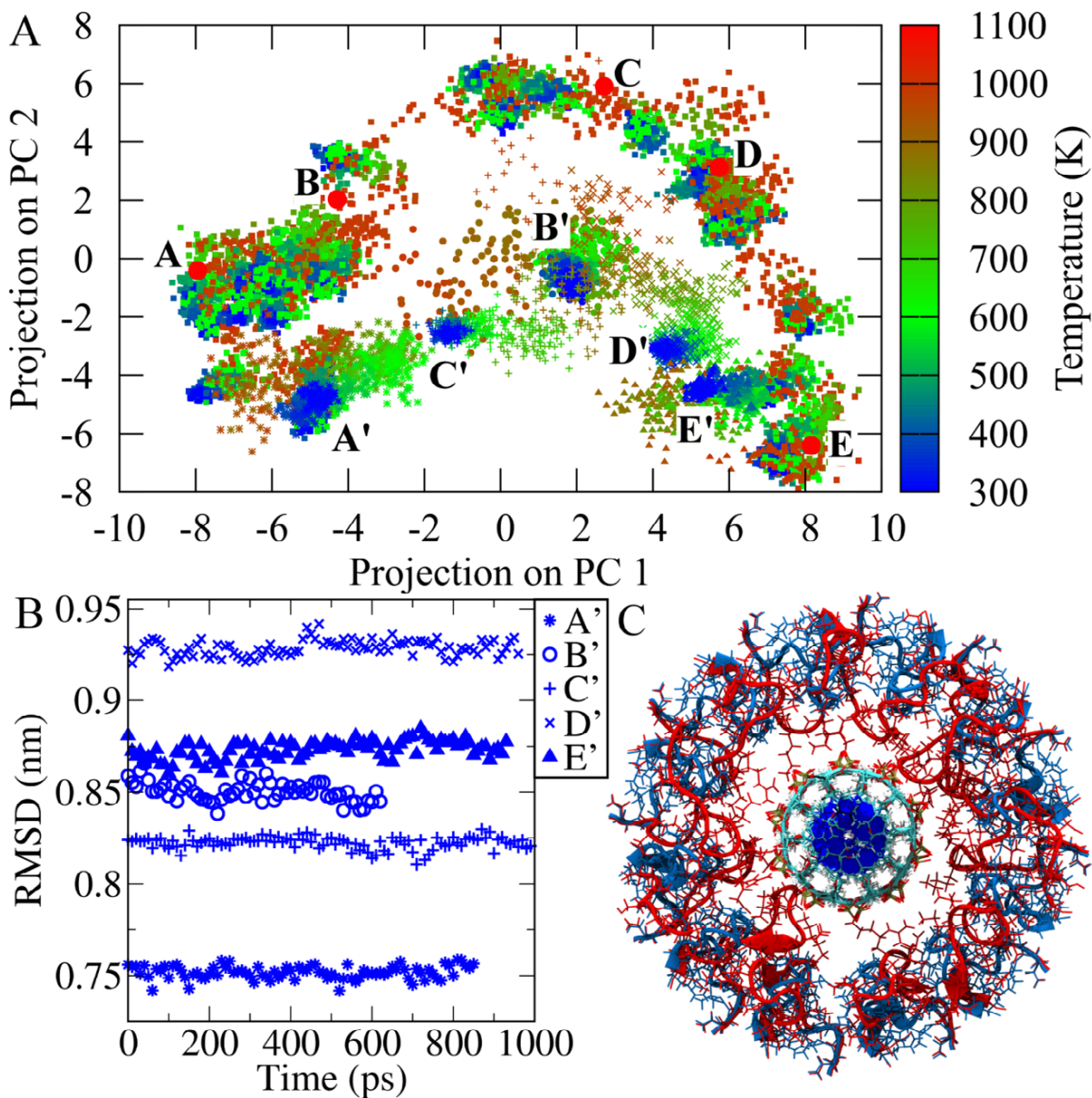
Figure S2: Refinement of the connector loops. (A) Plane of projection between first and second principal components (PC1 and PC2) obtained after performing PCA on the SA MD trajectories (*squares*). Five high temperature conformations A, B, C, D, and E (*red circles*) were selected from the projection plane and cooled down to 300 K. Dense clusters (*blue symbols*) labeled with A', B', C', D', and E' were obtained after cooling. (B) The structures of these five clusters (*blue symbols*) were compared by computing RMSDs of Cα atoms with reference to the starting loop structure models. (C) Comparison of modeled (*blue*) and refined loops (*red*) interacting with the DNA in the channel center.
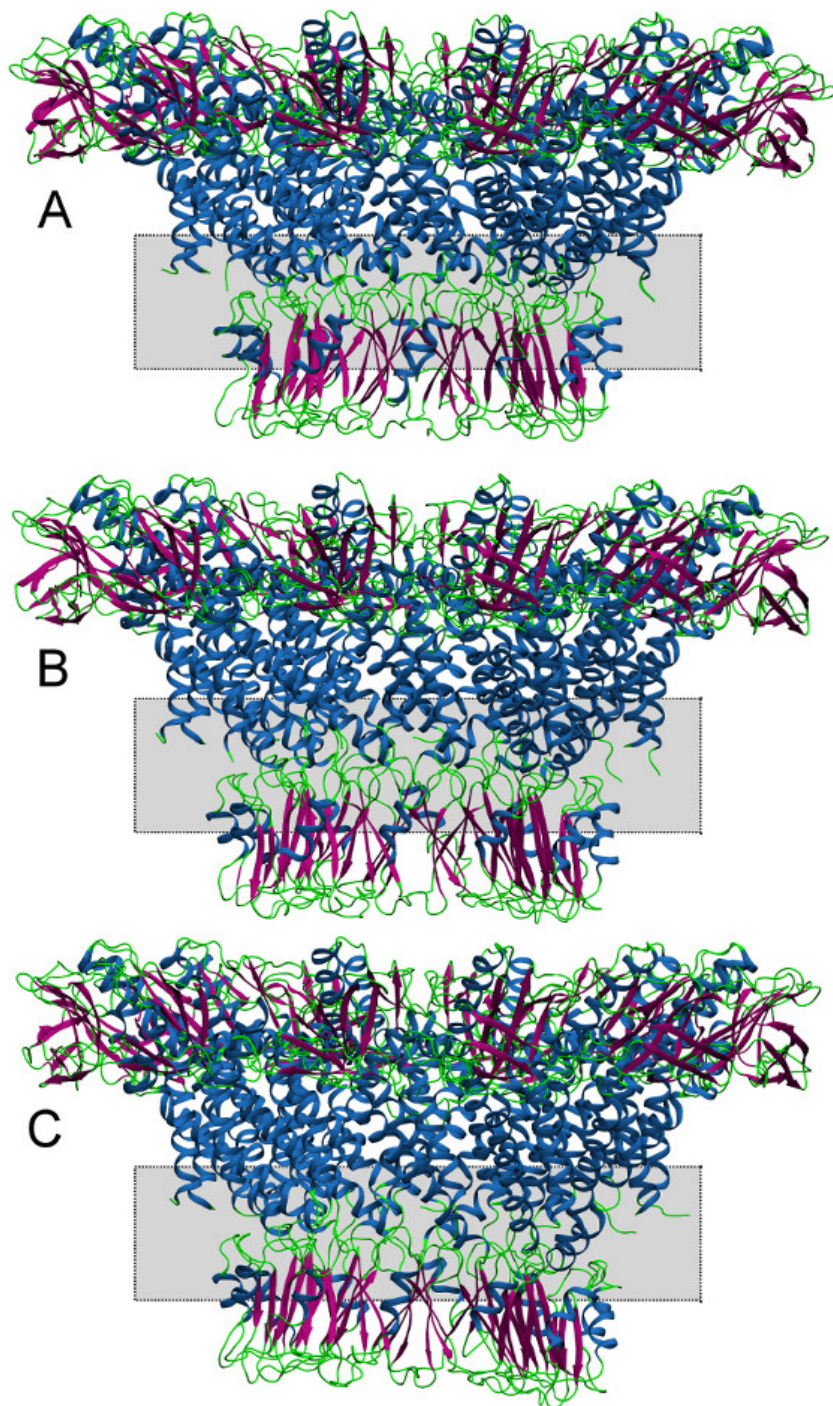
Figure S3: Starting non-equilibrium conformations used to characterize relaxation behaviors. Three non-equilibrium connector conformations of (A) 4.72 nm, (B) 5.1 nm, and (C) 5.3 nm length were selected for relaxation simulations. Region of structural deformations is shown as *shaded area*.
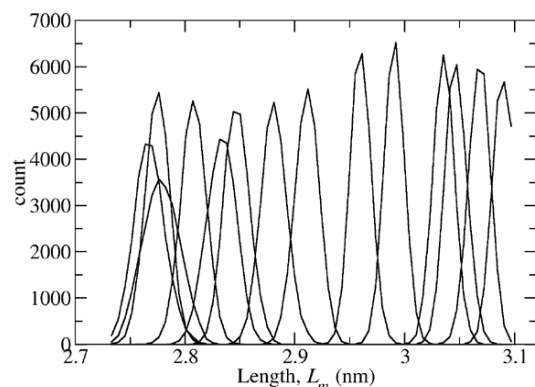
Figure S4: Collected histograms from compression-stretching umbrella sampling simulations. These histograms show the population of connector conformations along the reaction coordinate L_m during umbrella sampling simulations and were used to calculate the deformation free energy using WHAM (19-21).
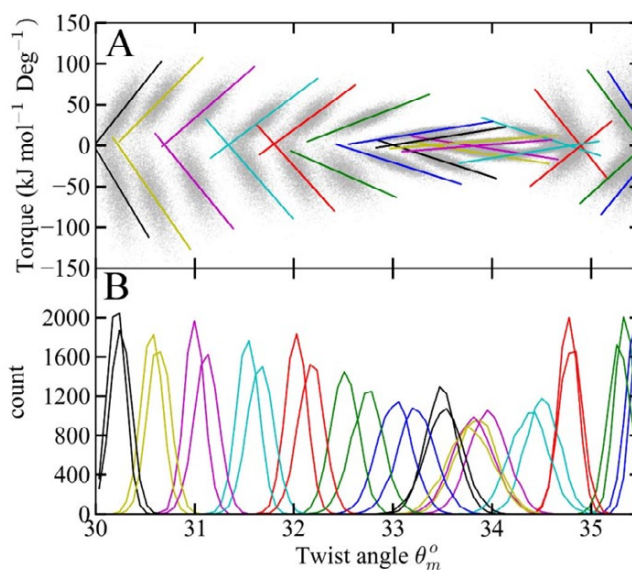
Figure S5: Torsional harmonic constants and collected histograms from twisting-untwisting umbrella sampling simulations. The group of atoms was harmonically restraint by applying a tangential harmonic force constant (kJ mol^{-1} nm^{-2}) during umbrella sampling simulations (15). Colors represent different sampling windows. The torsional harmonic force constants (kJ mol^{-1} deg^{-2}) were calculated from best line fits of the torque-twist angle values and were used to derive the deformation free energies for twisting-untwisting motions using WHAM (19-21). (A) Torque with respect to the twist angle θ_m during umbrella sampling simulations. Colored lines are the best fit lines of the respective sampling window. (B) Collected histograms showing the population of connector conformations along the reaction coordinate θ_m^o from each sampling window.
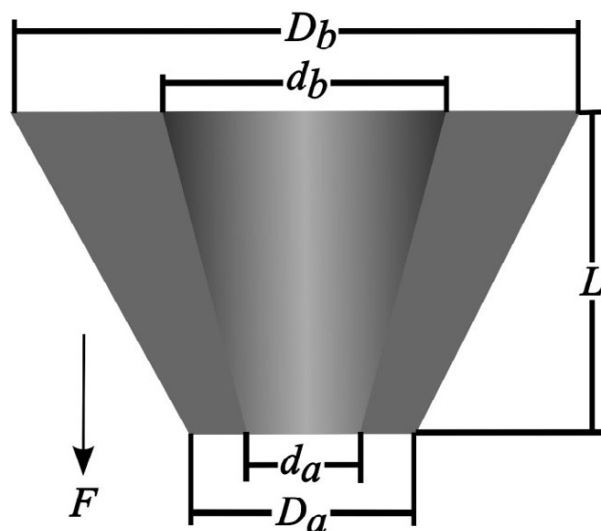
Figure S6: Geometrical characterization of the truncated hollow cone model used for calculating the Young's modulus of elasticity. The sketch shows the truncated hollow cone of length L, where D_a and d_a denote the narrow end exterior and interior diameter, respectively; D_b and d_b denote the wide end exterior and interior diameter, respectively. Equation 4 was derived on the basis of this model by assuming that the force F is acting in arrow direction.
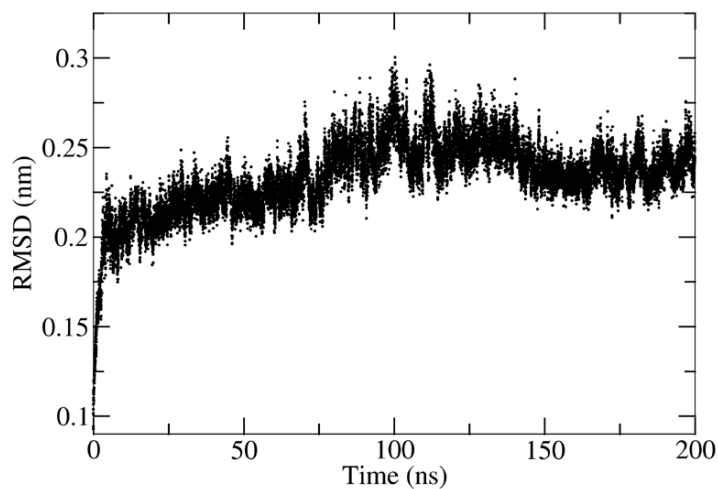

Figure S7: Root Mean Square Deviations of the connector from equilibrium simulations. RMSDs were calculated for Cα atoms of the connector with reference to the X-ray crystal structure (PDB ID: 1H5W).
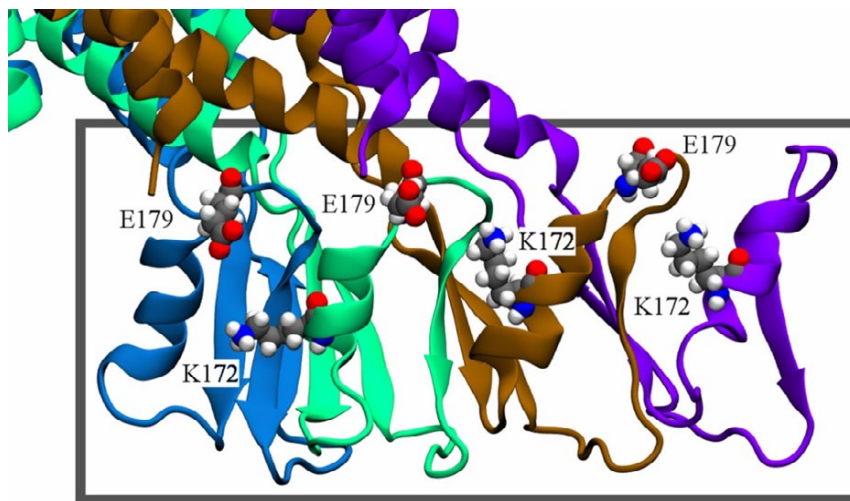
Figure S8: Deviations in twist angle during equilibrium simulations. During MD simulations, the twist angle of the connector deviated by 3.5° with respect to the crystal structure (PDB ID: 1H5W). The bottom connector region rotated with respect to the remaining part of the connector during the first 10 ns of the simulation. The grey box highlights the bottom region of four subunits that are depicted as colored cartoon representations. Residues E179 and K172 (*space-fill*) are mostly responsible for tilting of encasing α-helix.
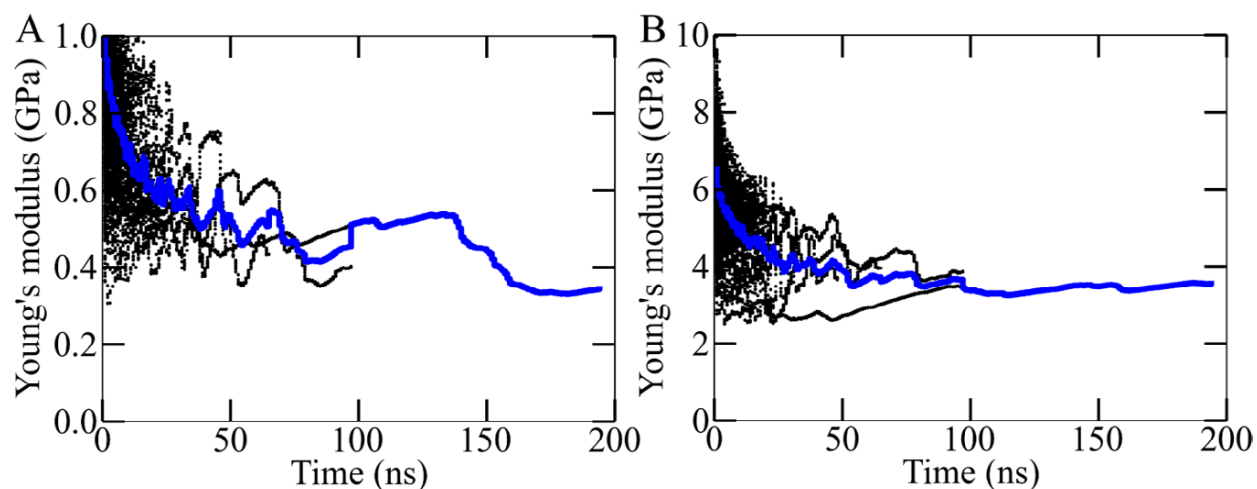

Figure S9: Convergence in the Young's modulus during the simulations. Both the time-blocks (black dots) as well as average (blue line) values of the Young's moduli with respect to the time are shown for (A) the whole connector and (B) the middle region. The moduli were calculated using Eq. 4 and, the required average of the dimensions (Fig. S6) over time and the stretching spring constant were obtained from non-overlapping time-blocks of the MD trajectory. The obtained modulus from each block is shown as a black dot. The average Young's modulus over the respective block size is shown as a blue solid line.
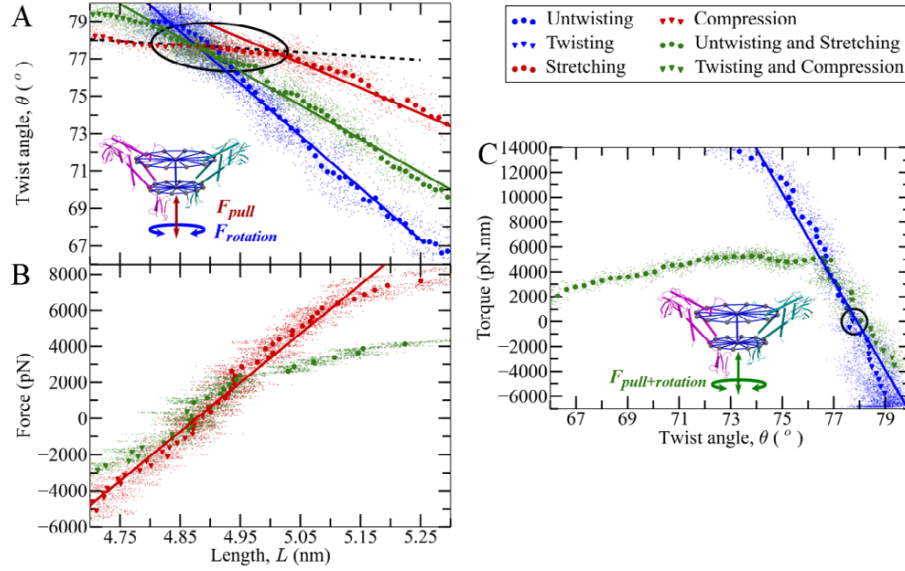
Figure S10: Elastic properties of the whole connector derived from force probe (FP) simulations; fluctuating instantaneous lengths and twist angles are shown as small dots, solid symbols represent averages over intervals in *x*-direction. The insets indicate pulling forces (F_{pull}) and torques ($F_{rotation}$) applied for different simulation sets FP-1/2 (*red arrow*), FP-3/4 (*blue arrow*), and FP-5/6 (*green arrows*) referred to in the text. (A) Enforced length change and/or twist: change in twist angle θ during enforced change of length L (*red*), length change during enforced twist/untwist (*blue*), twist angle and length change during simultaneous enforced twisting-compression and untwisting-stretching (*green*). The coupling between compression-stretching and untwisting-twisting motions during FP-1/2 (*red line*), FP-3/4 (*blue line*), and FP-5/6 (*green line*) is compared to the coupling (*black dashed line*) and the fluctuation range (*black ellipse*) obtained from equilibrium simulations. (B, C) Same data and coloring as (A), shown with applied force and torque and linear least square fits to the respective linear regime (lines). In (C), the black circle denotes the initial twist angle.
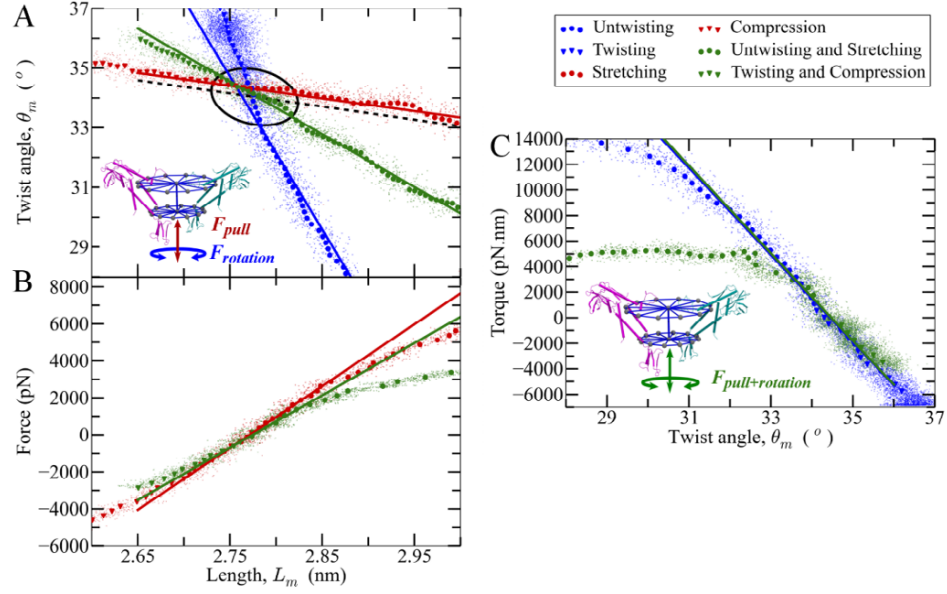
22

Figure S11: Elastic properties of the middle region derived from FP simulations; fluctuating instantaneous lengths and twist angles are shown as small dots, solid symbols represent averages over intervals in *x*-direction. Insets indicate applied pulling forces (F_{pull}) and torques ($F_{rotation}$) used in different simulation sets FP-1/2 (*red arrow*), FP-3/4 (*blue arrow*), and FP-5/6 (*green arrows*), as listed in Table S2. (A) Enforced length change and/or twist: change in twist angle θ during enforced change of length *L* (*red*), length change during enforced twist/untwist (*blue*), twist angle and length change during simultaneous enforced twisting-compression and untwisting-stretching (*green*). The coupling between compression-stretching and untwisting-twisting motions during FP-1/2 (*red line*), FP-3/4 (*blue line*), and FP-5/6 (*green line*) is compared to the coupling (*black dashed line*) and the fluctuation range (*black ellipse*) obtained from equilibrium simulations. (B, C) Same data and coloring as (A), shown with applied force or torque and linear least square fits to the respective linear regime (*lines*).
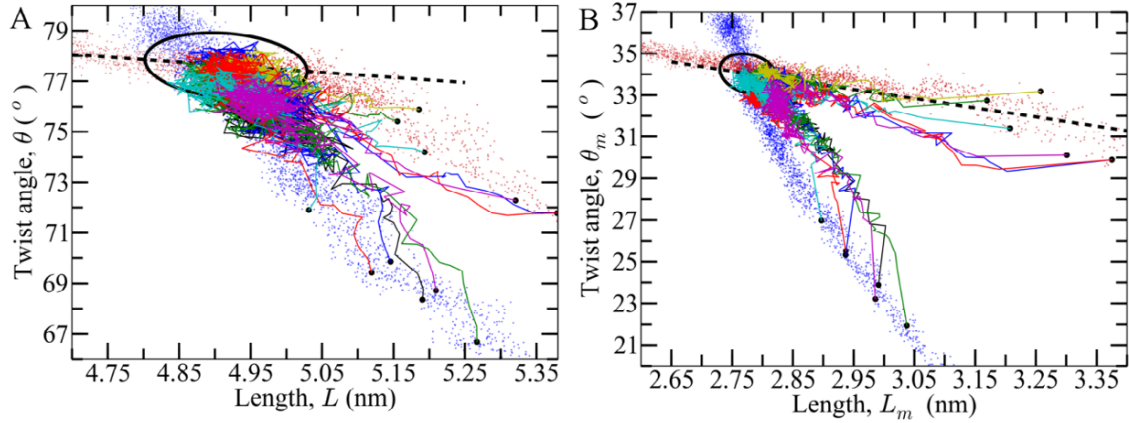
23

Figure S12: Convergence of relaxation paths towards an equilibrium. The comparison of relaxation paths (*colored lines*) with the obtained paths from enforced untwisting-only (*blue dots*) and stretching-only (*red dots*) motions for the (A) whole connector and (B) the middle region. Black dots denote starting non-equilibrium conformations taken from stretching simulation FP-2 (*red dots*) and untwisting simulation FP-4 (*blue dots*). To compare with equilibrium simulations, the range of fluctuations is denoted as black ellipse. Untwisting-stretching coupling is given by the slope of the best-fit line (*black dashed line*).
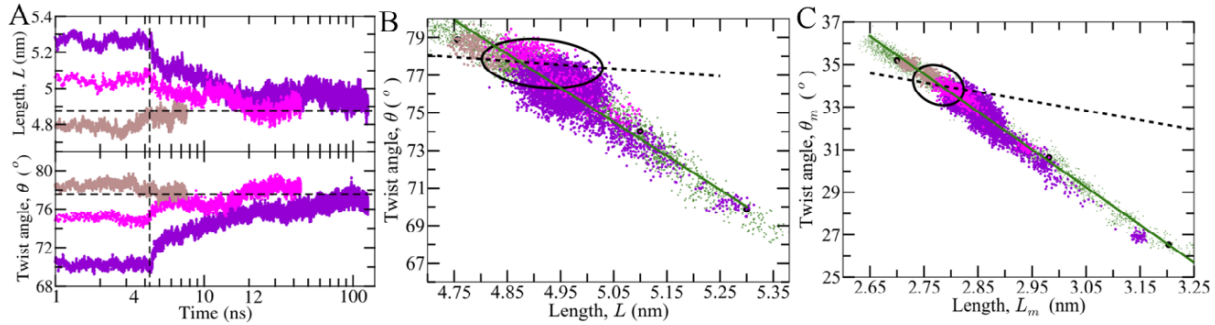

Figure S13: Reversible recovery of the equilibrium conformation. For three deformed connector structures with *L*=4.72, 5.1, and 5.3 nm (Figs. S3A-C), selected from simulations FP-5/6, their relaxation behavior (*purple*, *magenta,* and *light brown dots*) are illustrated. (A) The relaxation of connector's twist angle and length along the time towards the equilibrium structure (*horizontal dashed lines*) was observed for 120 ns (note the logarithmic scale). At 4.4 ns (*vertical dashed black line*) the restraint force was removed for complete relaxation. Relaxation pathways for (B) the whole connector and (C) the middle region towards the equilibrium structural fluctuations (*black ellipse*). Also, the comparisons of the relaxation paths with the obtained paths (green symbols and line) of untwisting-stretching motions from the same simulation set are shown. The coupling between compression-stretching and twisting-untwisting motions during FP-5/6 (*green line*) is compared to the coupling (*black dashed line*) obtained from the equilibrium simulations.
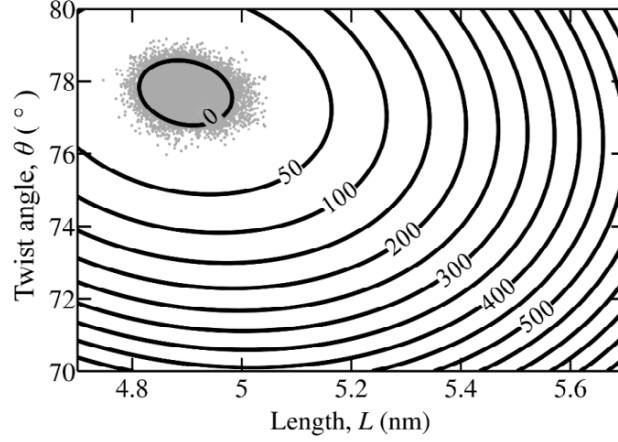
Figure S14: Free energy landscape from equilibrium fluctuations**.** The free energy of deformations for twisting-untwisting and compression-stretching motions was computed from equilibrium simulations under harmonic approximation of the energy landscape. The free energy (kJ/mol) was calculated from the probability density using the following equation $G(\theta, L) = -k_B T \ln[p(\theta, L)]$, where θ denotes the twist angle, L the length of the connector, k_B the Boltzmann constant, and T the temperature, respectively. The landscape was extrapolated beyond the equilibrium region to test the proposed untwist-twist DNA packaging mechanism.
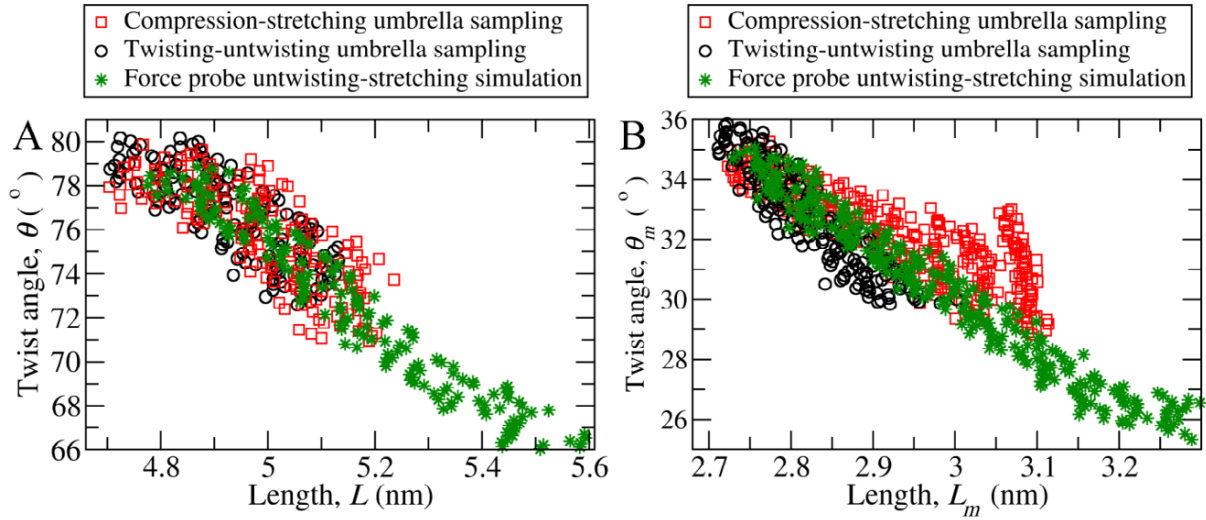

Figure S15: Convergence of deformation paths in umbrella sampling simulations. The pathways of untwisting-stretching motions were obtained from compression-stretching (*red squares*) and twisting-untwisting (*black circles*) umbrella sampling simulations and are compared to each other and to force probe simulation FP-6 (*green asterisks*) for (A) the whole connector and (B) the middle region.
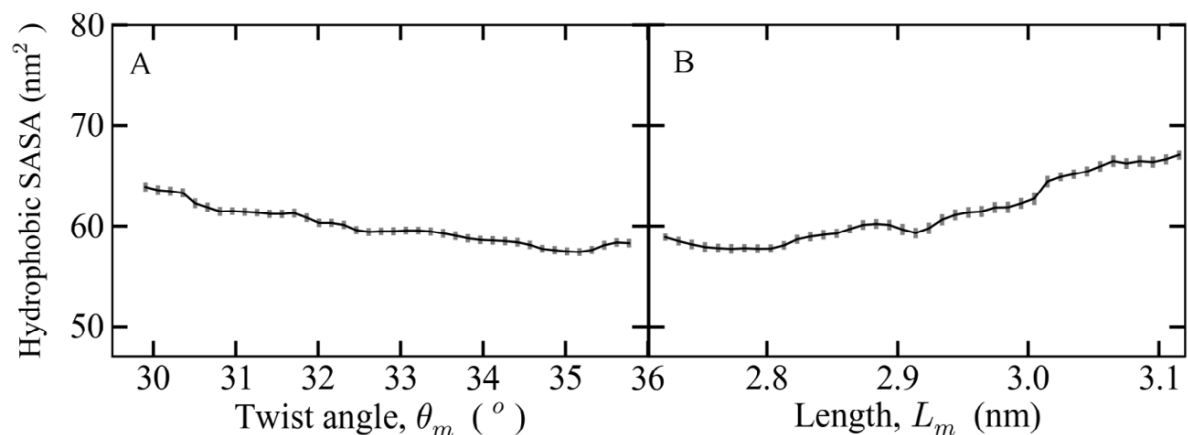
Figure S16: Deformation dependent changes in hydrophobic solvent accessible surface areas (SASAs) of the middle connector region derived from umbrella sampling simulations. Change in hydrophobic SASAs during (A) untwisting-stretching (twist angle θ_m) and (B) compression-stretching (length L_m) deformations. Hydrophobic SASAs were used to calculate the respective free energy. Error bars represent SE obtained from boot-strapping.
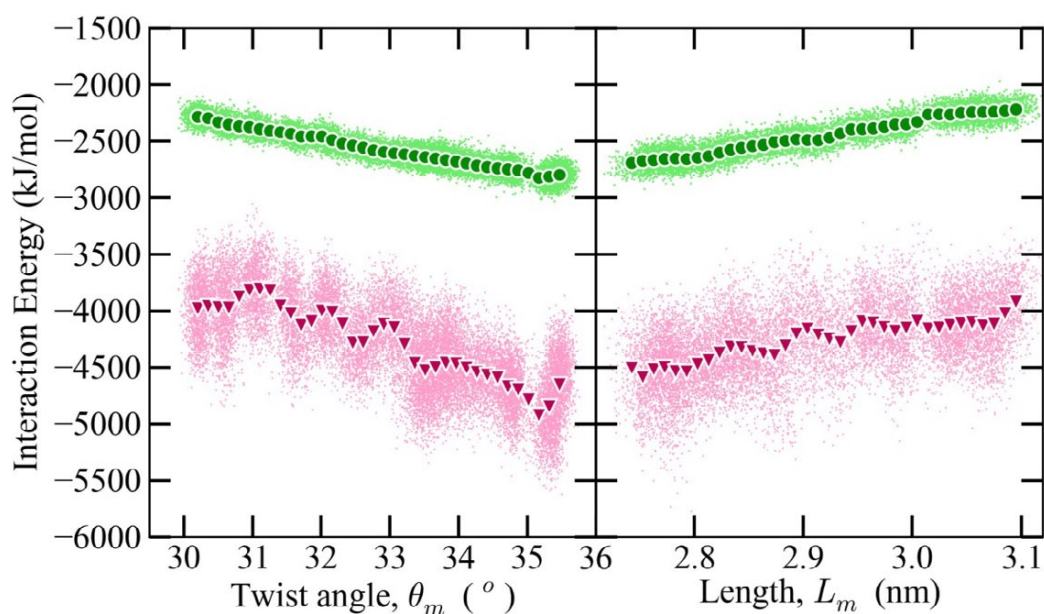

Figure S17: Residue packing dependent changes in interaction energies between deformed subunits of the middle connector region derived from umbrella sampling simulations. Fluctuating instantaneous interaction energies are shown as small dots; solid symbols represent averages over intervals in *x*-direction. Calculated van der Waals (*green circles*) and electrostatic (*red triangles*) interaction energies with respect to the deformation in (A) twist angle θ_m and (B) length L_m are depicted.

References

1.   Fernandez-Fuentes, N., J. Zhai, and A. Fiser. 2006. ArchPRED: a template based loop structure prediction server. Nucleic. Acids. Res. 34:W173-176.

2.   Eswar, N., B. Webb, M. A. Marti-Renom, M. S. Madhusudhan, D. Eramian, M. Y. Shen, U. Pieper, and A. Sali. 2007. Comparative protein structure modeling using MODELLER. Curr. Protoc. Protein. Sci. Chapter 2:Unit 2 9.

3.   Macke Thomas, J. and A. Case David. 1997. Modeling Unusual Nucleic Acid Structures. In Molecular Modeling of Nucleic Acids. American Chemical Society. 379-393.

4.   Hess, B., C. Kutzner, D. van der Spoel, and E. Lindahl. 2008. GROMACS 4: Algorithms for highly efficient, load-balanced, and scalable molecular simulation. J. Chem. Theory. Comput. 4:435-447.

5.   Hornak, V., R. Abel, A. Okur, B. Strockbine, A. Roitberg, and C. Simmerling. 2006. Comparison of multiple Amber force fields and development of improved protein backbone parameters. Proteins 65:712-725.

6.   Perez, A., I. Marchan, D. Svozil, J. Sponer, T. E. Cheatham, 3rd, C. A. Laughton, and M. Orozco. 2007. Refinement of the AMBER force field for nucleic acids: improving the description of alpha/gamma conformers. Biophys. J. 92:3817-3829.

7.   Berendsen, H. J. C., J. P. M. Postma, W. F. Vangunsteren, A. Dinola, and J. R. Haak. 1984. Molecular-Dynamics with Coupling to an External Bath. J. Chem. Phys. 81:3684-3690.

8.   Darden, T., D. York, and L. Pedersen. 1993. Particle Mesh Ewald - an N.Log(N) Method for Ewald Sums in Large Systems. J. Chem. Phys. 98:10089-10092.

9.   Amadei, A., A. B. Linssen, and H. J. Berendsen. 1993. Essential dynamics of proteins. Proteins 17:412-425.

10.   Berendsen, H. J. and S. Hayward. 2000. Collective protein dynamics in relation to function. Curr. Opin. Struct. Biol. 10:165-169.

11.   Garcia, A. E. 1992. Large-amplitude nonlinear motions in proteins. Phys. Rev. Lett. 68:2696-2699.

12.   Hayward, S., A. Kitao, F. Hirata, and N. Go. 1993. Effect of solvent on collective motions in globular protein. J. Mol. Biol. 234:1207-1217.

13.   Kitao, A., F. Hirata, and N. Gō. 1991. The effects of solvent on the conformation and the collective motions of protein: Normal mode analysis and molecular dynamics simulations of melittin in water and in vacuum. Chem. Phys. 158:447-472.

14.   Hess, B. 2000. Similarities between principal components of protein dynamics and random diffusion. Phys. Rev. E Stat. Phys. Plasmas. Fluids. Relat. Interdiscip. Topics 62:8438-8448.

15.   Kutzner, C., J. Czub, and H. Grubmuller. 2011. Keep It Flexible: Driving Macromolecular Rotary Motions in Atomistic Simulations with GROMACS. J. Chem. Theory. Comput. 7:1381-1393.

16. Kappel, C., N. Dolker, R. Kumar, M. Zink, U. Zachariae, and H. Grubmuller. 2012. Universal relaxation governs the nonequilibrium elasticity of biomolecules. Phys. Rev. Lett. 109:118304.

17. Simpson, A. A., Y. Tao, P. G. Leiman, M. O. Badasso, Y. He, P. J. Jardine, N. H. Olson, M. C. Morais, S. Grimes, D. L. Anderson, T. S. Baker, and M. G. Rossmann. 2000. Structure of the bacteriophage phi29 DNA packaging motor. Nature 408:745-750.

18.   Hess, B. 2002. Determining the shear viscosity of model liquids from molecular dynamics simulations. J. Chem. Phys. 116:209-217.

19. Hub, J. S., B. L. de Groot, and D. van der Spoel. 2010. g_wham-A Free Weighted Histogram Analysis Implementation Including Robust Error and Autocorrelation Estimates. J. Chem. Theory. Comput. 6:3713-3720.

20. Kumar, S., D. Bouzida, R. H. Swendsen, P. A. Kollman, and J. M. Rosenberg. 1992. The Weighted Histogram Analysis Method for Free-Energy Calculations on Biomolecules .1. The Method. J. Comput. Chem. 13:1011-1021.

21. Roux, B. 1995. The Calculation of the Potential of Mean Force Using Computer-Simulations. Comput. Phys. Commun. 91:275-282.